11
X-Ray Diffraction Analysis of Elastic Strains at the Nanoscale

Olivier Thomas, Odile Robach, Stéphanie Escoubas, Jean-Sébastien Micha, Nicolas Vaxelaire, and Olivier Perroud

11.1
Introduction

It is well established that X-ray diffraction (XRD) is perfectly suited to analyze strains in crystals [1]. The sensitivity of XRD to the position of atoms together with the high resolution that may be achieved in diffraction space is the basis of structure solving. On the other hand, the size of conventional X-ray beams (100 μm–1 mm) prevented until recently any local strain determination relying on direct space resolution. During the past 10 years developments in X-ray optics [2] and in X-ray sources have paved the way for micro- or nanobeam diffraction [3] (expectations lie around 50 nm). With respect to electron beams, X-ray beams are clearly lagging behind when it comes to beam size and thus direct space resolution. But X-rays have a strong advantage: they are basically nondestructive and yield information on buried structures without any need for special sample preparation, which may drastically alter the original strain field in the sample. Moreover, as already mentioned, the limited real space resolution may be circumvented in some cases by reciprocal space resolution (a 5 nm resolution has been reported in Ref. [4]).

With the development of nanoscience and nanotechnologies, the need for high-resolution strain measurements at scales as small as possible has become an important issue. Because yield strengths are significantly higher in small dimensions [5], stresses play an important role in the unusual properties often encountered at small scales [6]. In technology and more specifically in microelectronics, the ability to measure strains in small features is critical. In small Cu interconnects, local stresses may trigger phenomena such as stress-induced voiding [7] that is one of the reasons for the failure of devices. In the very core of the transistors, the stress in the Si channel (32 nm wide in emerging technologies) is a tunable parameter to control the mobility of charge carriers [8].

This chapter is aimed at reviewing recent advances in local strain determination using XRD. A brief reminder of the basics of XRD within the framework of kinematic approximation is given in Section 11.2. Section 11.3 focuses on average strain

Mechanical Stress on the Nanoscale: Simulation, Material Systems and Characterization Techniques, First Edition. Edited by Margrit Hanbücken, Pierre Müller, and Ralf B. Wehrspohn.

measurements from Bragg peak shifts. Section 11.4 is devoted to submicron-sized X-ray beams and their use for local strain measurements. In Section 11.5, we address the issue of strain determination from the distribution of intensity in reciprocal space. The specific issue of periodic systems is considered where the periodicity is used to enhance the diffracted signal from a single period and hence yield local information on the strain field. Coherent diffraction, a very promising technique for determining strains in single nanocrystals, is also described. Section 11.6 briefly addresses the issue of phase retrieval, which is a way to invert directly the diffracted signal and thus obtain the displacement field without any *a priori* model.

11.2
Strain Field from Intensity Maps around Bragg Peaks

We will first consider the simplest situation where an incident, fully coherent monochromatic X-ray beam with wavelength λ is scattered elastically by a crystal. The interaction of X-rays with matter is very weak, and this allows the scattered amplitude to be written as a simple Fourier transform [9] of the electron density

$$A(\vec{q}) = \int \varrho(\vec{r}) e^{i\vec{q}.\vec{r}} d\vec{r} \tag{11.1}$$

where $\varrho(\vec{r})$ is electron density in real space and $\vec{q} = \vec{k}_f - \vec{k}_i$ is the scattering vector defined as the difference between the incident wave vector and the scattered one. The modulus of $\vec{q}$ is simply related to the scattering angle 2θ

$$q = \frac{4\pi}{\lambda} \sin\theta \tag{11.2}$$

where λ is the wavelength of the incoming radiation.

Formula (11.1) remains an approximation and in the case of perfect crystals, it should be carefully justified. Generally, thin crystals with thickness smaller than the extinction length scatter waves in the kinematic regime [10]. For crystals larger than the extinction length, it is the crystal quality (mosaicity, density of defects, etc.) that will determine whether they scatter in the kinematic or dynamic regime.

In the case of a crystal, considering the Bravais lattice $\vec{R}_m$ and the shape function $s(\vec{r})$, one gets

$$A(\vec{q}) = \mathrm{TF}\left[s(\vec{r}) \sum_m \varrho_c(\vec{r}) * \delta(\vec{r} - \vec{R}_m) \right] = S(\vec{q}) * F(\vec{q}) \sum_m e^{i\vec{q}\cdot\vec{R}_m} \propto S(\vec{q}) * F(\vec{q}) \sum_m \delta(\vec{q} - \vec{G}_m) \tag{11.3}$$

where $\varrho_c(\vec{r})$ is the unit cell electron density, $F(\vec{q})$ its Fourier transform, that is, the structure factor, $S(\vec{q})$ is the Fourier transform of $s(\vec{r})$, and $\vec{G}_m$ are reciprocal space vectors. This very well-known expression shows simply that the diffraction pattern of an unstrained crystal consists in well-defined Bragg peaks at positions given by the Laue condition: $\vec{q} = \vec{G}_m$. Moreover, the Fourier transform $S(\vec{q})$ of the crystal shape is

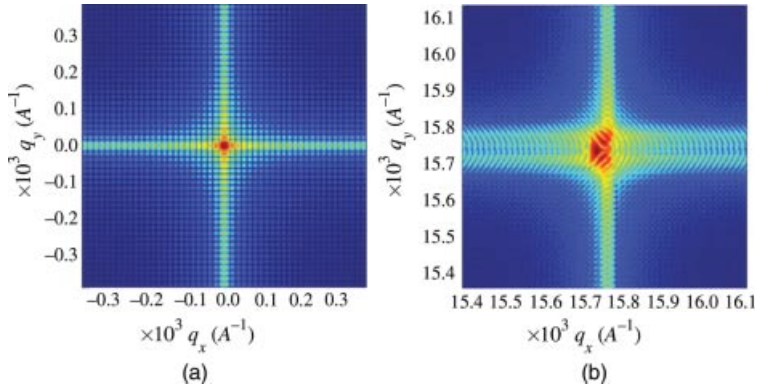

Figure 11.1 Coherent diffraction pattern from a square crystal calculated within the kinematic approximation. (a) At the origin of reciprocal space, the influence of crystal size is solely visible. (b) Around Bragg reflection, strain in the crystal distorts the diffraction pattern.

transferred by convolution on any reciprocal space node. Figure 11.1a shows the modulus $|S(\vec{q})|$ for a simple 2D square crystal. Periodic fringes are related to the size of the crystal, while streaks occur along the normal to the facets.

Let us consider now the case of a strained crystal [11]. We will restrict ourselves in the first step to purely elastic strains. Moreover, considering that elasticity in crystals can only describe the distortion of the lattice [12] (and not of the basis) and that elastic strains are always small (even in nanocrystals they remain of the order of a few percent), we will assume that the structure factor $F(\vec{q})$ remains unchanged. In the strained crystal, the lattice is distorted

$$\vec{R}' = \vec{R} + \vec{u} \tag{11.4}$$

where $\vec{u}$ is the displacement field. It is worth noting that diffraction is sensitive to the displacement and not simply to the strain, that is, diffraction is also highly sensitive to lattice rotation. If $i = 1, 2, 3$ are the principal orthogonal directions in space, the strain and rotation tensors [13] ε_{ij} and ω_{ij} are written as

$$\varepsilon_{ij} = \frac{1}{2}\left(\frac{\partial u_i}{\partial x_j} + \frac{\partial u_j}{\partial x_i}\right) \text{ and } \omega_{ij} = \frac{1}{2}\left(\frac{\partial u_i}{\partial x_j} - \frac{\partial u_j}{\partial x_i}\right) \tag{11.5}$$

within the framework of the small displacements approximation.

The amplitude scattered from the strained crystal is written now as

$$A(\vec{q}) = S(\vec{q}) * F(\vec{q}) \sum_m e^{i\vec{q}\cdot(\vec{R}_m + \vec{u}_m)} \tag{11.6}$$

In the vicinity of Bragg peak $\vec{G}_{hkl}$, one may write $\vec{q} = \vec{G} + \vec{g}$ and neglect the term $\vec{g} \cdot \vec{u}$. Thus,

$$A(\vec{q}) \approx S(\vec{q}) * F(\vec{q}) \sum_m e^{i\vec{G}_{hkl}\vec{u}_m} \cdot e^{i\vec{q}\cdot\vec{R}_m} \tag{11.7}$$

This shows that the amplitude scattered by the strained crystal may be described to a very good approximation [14] as the Fourier transform of a modified electron density:

$$A(\vec{q}) \approx \mathrm{TF}[\varrho(\vec{r})\mathrm{e}^{i\vec{G}_{\mathrm{hkl}}\cdot\vec{u}(\vec{r})}] \tag{11.8}$$

In consequence, a strained crystal behaves as if it had a complex electron density with a phase factor $\vec{G}_{\mathrm{hkl}} \cdot \vec{u}(\vec{r})$. This phase strongly influences the intensity distribution as shown, for example, in Figure 11.1b where a displacement field has been introduced in the previous square crystal. Because the phase field considered here is not centrosymmetric, the diffraction pattern does not remain centrosymmetric, that is, Friedel's law is not valid any more. The corresponding asymmetry in the diffraction pattern is a good sign for the presence of a strain field within the crystal. One should, however, remember that a centrosymmetric phase field would yield a centrosymmetric diffraction pattern. Hence, a strained crystal may still have a symmetric diffraction pattern.

At variance with the size effect previously described, this strain effect is clearly Bragg peak dependent. When the strain is homogeneous throughout the crystal under investigation, the displacement field varies linearly with position and the amplitude remains unaffected. The strain is then deduced directly from the shift in peak position. This forms the basis of many methods to determine strains and stresses in materials.

The examples illustrated in Figure 11.1 are typical of what is conventionally named coherent X-ray diffraction (CXD) where a crystal is illuminated by a fully coherent beam. The coherence length depends heavily on the source and optics used. The longitudinal coherence length is related to the energy spread in the beam. Typically, a Si(111) monochromator yields an energy spread of 10^{-4}, hence a longitudinal coherence length of 1 μm at 8 keV. The transverse coherence length is inversely related to the source size. On third-generation synchrotron source, it may reach 100 μm; but on laboratory setups, 1 μm is an upper limit that calls for a very small divergence.

When the beam size is larger than the coherence length, the intensity on the detector is an incoherent addition of intensities scattered by different parts of the sample under the beam. Because of the dispersion in size, strains, and so on in the beam footprint, one does not observe fringes any more but a diffraction peak whose width may be related to the average size distribution and strain distribution standard deviation.

11.3
Average Strains from Diffraction Peak Shift

Under Bragg conditions $q = G_{hkl} = 2\pi/d_{hkl}$, where d_{hkl} is the interplanar spacing. One can then derive the corresponding strain from the knowledge of the strain-free spacing d^0_{hkl}

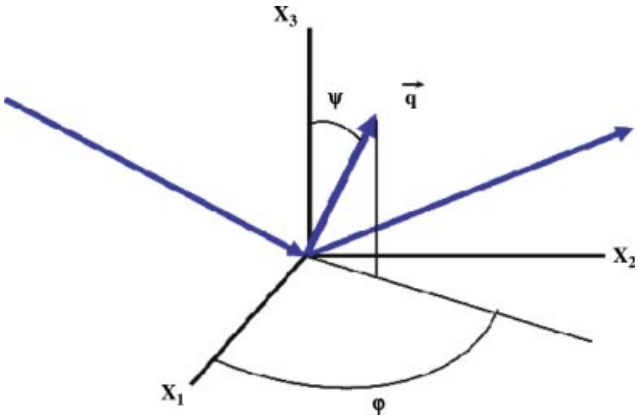

Figure 11.2 Diffraction geometry and scattering vector.

$$\varepsilon = \frac{d_{hkl} - d^0_{hkl}}{d^0_{hkl}} \tag{11.9}$$

The change in the length of the scattering vector can be written as

$$\delta q = q - q_0 = \varepsilon q \tag{11.10}$$

This shows that much better accuracy is obtained for large qs, that is, for large scattering angles.

On a four-circle diffractometer, q-values may be measured with different orientations ψ and φ with respect to the surface normal (Figure 11.2).

The corresponding strain is thus measured in a reference frame that has been rotated with respect to the sample's reference frame. Performing the proper tensor rotation (strain is a symmetric second-rank tensor) yields

$$\begin{aligned} \varepsilon_{\phi\psi} = \; & \varepsilon^S_{11}\cos^2\varphi \sin^2\psi + \varepsilon^S_{12}\sin 2\varphi \sin^2\psi + \varepsilon^S_{22}\sin^2\varphi \sin^2\psi \\ & + \varepsilon^S_{33}\cos^2\psi + \varepsilon^S_{13}\cos\varphi \sin 2\psi + \varepsilon^S_{23}\sin\varphi \sin 2\psi \end{aligned} \tag{11.11}$$

where ε^S_{ij} refers to the strain tensor components in the sample's reference frame. Thus, the measurement of a large number of Bragg peak positions for different values of ψ and φ provides a powerful and accurate means of determining the full strain tensor.

In the simple case of an equal biaxial stress state, often encountered in thin films (here x_3 is taken as the surface normal), there is no dependence on the in-plane azimuth φ and the strain along ψ writes

$$\varepsilon_\psi = \varepsilon_{//}\sin^2\psi + \varepsilon_\perp\cos^2\psi \tag{11.12}$$

where $\varepsilon^s_{11} = \varepsilon^s_{22} = \varepsilon_{//}$ and $\varepsilon^s_{33} = \varepsilon_\perp$.

Equation (11.12) shows that $\varepsilon_\psi(\sin^2\psi)$ is a straight line whose slope yields directly the in-plane stress σ. This is the so-called $\sin^2\psi$ technique [1]. Moreover, there is a particular direction ψ_0 for which strain is zero and which depends solely on the

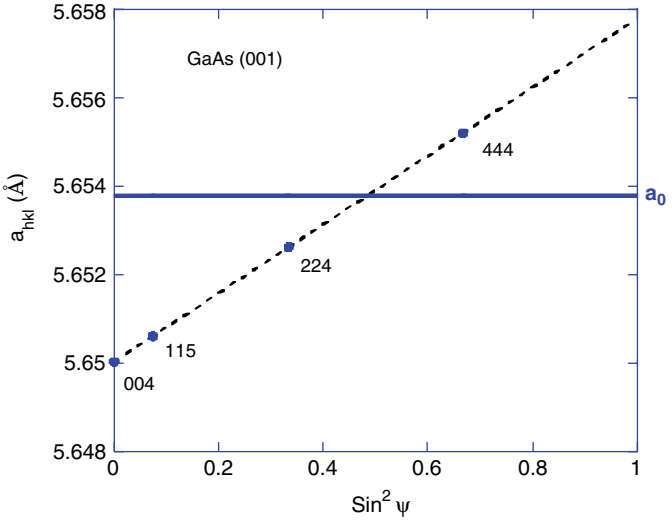

Figure 11.3 $Sin^2\psi$ plot from an epitaxial GaAs layer on Ge(001).

material's elastic constants. For a cubic material, measurement of lattice parameter at ψ_0 yields directly the stress-free lattice parameter a_0.

A typical example of a $\sin^2\psi$ plots can be found in Figure 11.3, where measurements taken [15] from an epitaxial GaAs layer grown on Ge(001) are shown. The slope indicates that the GaAs film is under tension. It is worth noting that what is actually measured with diffraction is the displacement field. The transition from displacement to strain requires the knowledge of strain-free lattice parameters [16], which may differ from bulk values because of the presence of impurities.

X-ray diffraction and Eq. (11.11) may be used to investigate more complex stress states [17] as encountered, for example, in trenches where a triaxial stress state occurs.

The transition from strain to stress is straightforward in the case of a single crystal since it requires the use of Hooke's law with proper provision for anisotropic elasticity. In the case of polycrystals, it is more delicate since a proper account of the way X-ray diffraction averages over different grain populations together with a mechanical model for grain interaction [18] should be used. Let us consider a very simple example of a Cu thin film with two types of grains: {100} and {111}. Cu is highly anisotropic with an anisotropy factor $A = 3.2$. It is thus expected that large grain-to-grain strain variations occur in such a film. Two extreme cases may be considered: (i) all grains are in the same state of stress (Reuss approximation) and (ii) all grains are in the same state of strain (Voigt approximation). The corresponding $\sin^2\psi$ plots are shown in Figure 11.4. These extreme cases do not satisfy basic compatibility requirements for the fields. One should therefore look for more elaborate models (self-coherent approaches do respect compatibility requirements). It is, however, clear that mean field approaches, which do not take into account the exact environment of a given grain, are borne to miss the exact distribution of strains within the film.

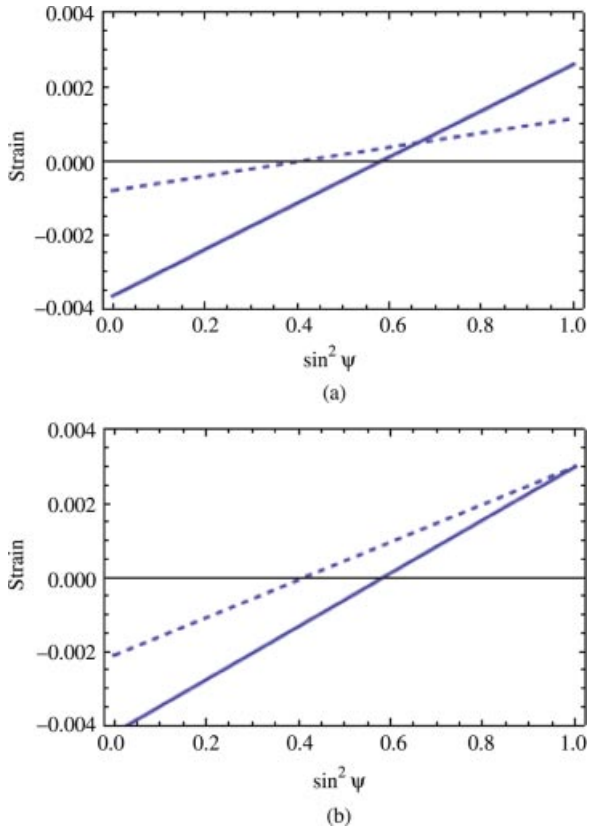

Figure 11.4 Calculated $Sin^2\psi$ plots for (111) Cu grains (dashed line) and (001) grains (solid line) in the Reuss (a) or Voigt (b) approximation.

Using "conventional" X-ray beam sizes in the range 100–1000 μm, it is average quantities that are determined from X-ray diffraction. Since strain fields are most often highly inhomogeneous on short length scales, the diffracted intensity will result from an incoherent addition of intensities scattered from areas with different strain levels. This results in a broadening of Bragg peaks, and a considerable amount of work [19] has been devoted to what is called line profile analysis (LPA), which is mostly aimed at extracting the second moment of the strain distribution from the width of Bragg peaks. The major difficulty arises when different sources of strain inhomogeneity are present at the same time (dislocations, boundary conditions, elastic anisotropy, etc.).

How can one determine the strain field at a scale as local as possible? The most obvious approach is to decrease the size of the X-ray beam in order to analyze as small an area as possible and monitor the average strain within the beam footprint via shifts in diffraction peaks. This is described in the next section.

11.4
Local Strains Using Submicrometer Beams and Scanning XRD

11.4.1
Introduction

The comprehension of complex crystalline materials (e.g., polycrystalline and/or multiphased), and their inhomogeneous distributions of stress and plastic deformation, requires microprobe techniques. Two X-ray diffraction techniques will be addressed here, 3DXRD [20, 21] and Laue microdiffraction [22, 23].

The physical meaning, in real space, of the objects dealt with, and of the quantities measured, when using microprobe X-ray diffraction, first need to be reminded.

Concerning space averages, diffraction is very sensitive to well-crystallized parts of the material, and very little sensitive to poorly crystallized parts: it acts as a filter of order. Any measured average of a quantity over the probed volume is therefore a "diffraction-wise" average, essentially a space average weighted by the degree of order. This needs to be taken into account when comparing "measured" strain with strain derived from a simulation of the displacement field.

Here we define a grain as one orientation of the crystal unit cell, with a certain angular tolerance, inside the probe volume. A grain can contain several well-crystallized domains separated by defective and/or differently oriented regions. The intragrain orientation distribution either may come from lattice curvature inside the well-crystallized domains or may come from rotations between the domains. When translating the material with respect to an X-ray microbeam, this angular tolerance is necessary to sort grains encountered at different positions of the probed volume according to their orientation, to draw the frontiers of the grains.

The "local elastic stress" measurements consist in using the well-crystallized domains of a grain as "ideal" small local stress sensors, dispersed inside a possibly much less ideal material. An extreme example would be small diamond single crystals dispersed in a matrix of amorphous glass. The sensors react to stress with the elastic rigidity tensor of the macroscopic single crystal. This hypothesis allows converting the measured lattice parameters, and the derived strain tensor, into a local elastic stress tensor.

In practice, the level of accuracy on strain (10^{-4}) required for useful mechanical measurements often implies that the center-of-mass positions of the diffraction spots (which serve as input for deriving the lattice parameters) need to be determined with an uncertainty much smaller than the spot width. This accuracy is accessible for simple spot shapes, but it becomes much more problematic when spots are asymmetric or split, which is often the case for plastically deformed materials. In such cases, spot shape analysis and simulation in terms of microdisorientation and microstrain inside the probe volume are necessary to locate the average spots and derive the average lattice parameters with a reasonable accuracy.

We will now describe how the two techniques proceed to map the positions, orientations, and elastic strain of the grains inside a polycrystalline material.

11.4.2
High-Energy Monochromatic Beam: 3DXRD

The methodology for 3DXRD was developed by the group of H.F. Poulsen using two high-energy beamlines: ID11 at ESRF (Grenoble, France) and 1-ID at APS (Argonne, IL, USA).

The basic version of 3DXRD allows to locate in 3D the center of mass (CM) of the grains and to determine their orientation, in the volume of a thick (a few millimeters to centimeters) polycrystal, with a spatial resolution around 5 μm. For successful measurements, the grains along the beam path should all be illuminated (sufficient transparency), in small numbers (<1000) and with low plastic deformation. Enhanced versions of the technique also allow to obtain (1) the full strain tensor of the grains and (2) a 3D reconstruction of the grain boundaries, for grains with low plastic strain.

Thanks to the high-energy X-ray beams (50–100 keV), small diffraction angles are obtained and allow to collect several $\{HKL\}$ rings from a powder diffraction pattern with a 2D detector and to explore the almost complete[1)] pole figures with only one sample rotation axis ω (Figure 11.5).

This statistical texture measurement can be extended to a grain-by-grain texture measurement when the number of diffracting grains for a given ω is small enough for the continuous Debye rings to become "granular." As ω rotates, a single grain will send diffracted beams into the different rings of the powder pattern. The first step of the analysis is to sort the list of (y, z, ω) peak positions derived from the N patterns measured at the N values of ω, to group together the spots coming from the same grain and index them (i.e., find their HKLs). This sorting is performed by the GRAINDEX program [20], now available for download on the SourceForge web site, thanks to the TotalCryst project, as part of the FABLE software [24]. Note that the monochromatic beam readily provides the $\{HKL\}$ family of a spot from its 2θ value (i.e., its ring number), which greatly facilitates the indexation. The maximum number of simultaneously illuminated grains is fixed by the need of separating the spots produced by the different grains for the indexation: it decreases when the spots are broader.

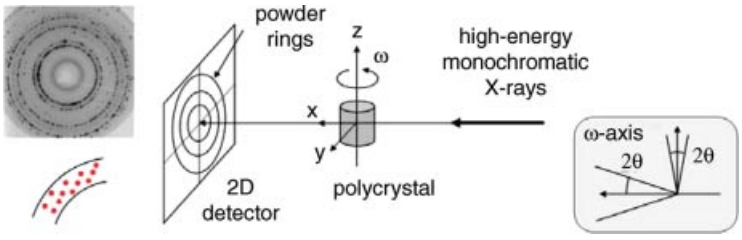

Figure 11.5 3D X-ray diffraction geometry: grain-to-grain texture analysis.

1) Save for a cone of angle $2\theta_{HKL}$ around the ω-axis.

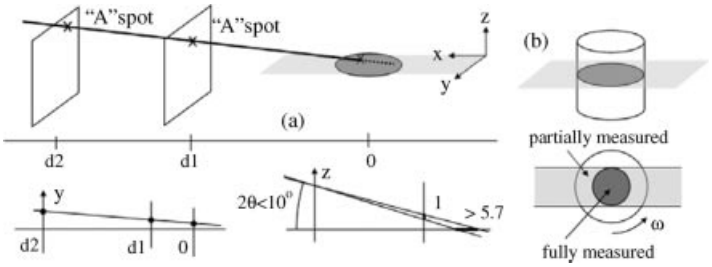

Figure 11.6 3DXRD: (a) triangulation method (two 2D detectors + planar beam) for locating the center of mass of a grain and (b) the sample periphery as a source of parasitic spots.

The method for locating the diffracting grains is described in Figure 11.6. The locating is first performed in 2D, in a horizontal (x, y, $z = z_0$) slice of the sample. The operation is then repeated for several slices at different z-values, providing the 3D position of the grain's CM.

The sample slice is illuminated by a planar beam, around 5 μm high and a few millimeters wide. At each value of ω, two powder patterns are recorded, one with a semitransparent 2D detector close to the sample and the second with a 2D detector far from the sample. After indexing the patterns taken at the detector positions d_1 and d_2, the equation of each diffracted ray and its point of intersection with the planar beam can be calculated. This gives the (x, y) position of the CM of the diffracting grain. At this stage, one can test if the various diffracted rays attributed to a given grain diverge from the same source point, to check the spot-sorting process. Each of these rays provides an independent determination of the source point position, which helps reduce the incertitude.

To reach the desired accuracy of 5 μm on (x, y), the first detector needs to be as close as possible to the sample (small $d_1 \approx 4$ mm) and to have a high spatial resolution (pixel size $\approx$2.5 μm). The smallness of the 2θ angles ($<10°$) makes this particularly necessary for the x-position, along the beam. An incertitude on the z-position of the spot at d_1 translates into an incertitude on x that is $1/\tan(2\theta)$ (>5.7) times larger.

The sample size should be adapted in order to be always fully illuminated by the horizontal section of the sample with the beam (Figure 11.6b). Otherwise, the spots coming from the periphery of the sample will not be exploitable and will only overcrowd the diagram and slow down the image analysis and indexation processes.

With this method, the orientation of each grain is determined, as well as the position of its CM, first in 2D and then in 3D.

The full elastic strain tensor (i.e., the six components), averaged over a 5 μm-thick slice at $z = z_0$ of the grain, can then be determined by two methods [25]. In the first method, only the 2θ positions of the spots are used and compared to their theoretical values for a strain-free sample, that is, strain (six parameters) is determined independent of orientation (three parameters). A minimum of six (HKL) spots are needed, with 3×3 linearly independent $\mathbf{q}$-vectors. The required high accuracy on 2θ is achieved by (1) using the largest possible sample-to-2nd detector distance d_2, (2) simultaneously locating the grain's CM by ray tracing, and (3) carefully calibrating the

experimental geometry (incident beam/detectors 1 and 2) using the diffraction pattern of a strain-free sample.

In the second method, the full angular information about each diffracted ray, including the ω sample rotation, is used to calculate the coordinates of the **q**-vector in the sample frame.

The **q**-vectors of at least four peaks (3×3 linearly independent) are then used to derive the full nine-component tensor giving the coordinates of the $\mathbf{a}^*$, $\mathbf{b}^*$, $\mathbf{c}^*$ vectors in the sample frame, that is, strain and orientation are refined simultaneously. The main difference is that here the ω angle is explicitly used in the matrix calculation, while in the first method it is used only when checking that the grain's CM is at the same position in the sample for all diffracted rays.

Finally, the use of a third 2D detector, semitransparent and close to the sample, is under development on ID11 at ESRF [26] to separate the spot broadening due to plastic deformation (which increases with detector distance) from the one due to grain shape (which is best seen at small detector distances, before beam divergence due to plastic deformation distorts the projection). The goal is to exploit the spot shape even for plastically deformed samples, to derive both the grain boundary maps [27, 28] and the intragrain orientation distribution function [29].

11.4.3
White Beam: Laue Microdiffraction

Laue diffraction is originally known mainly as a method to orient single crystals, thanks to the ability of a white (i.e., broadband) X-ray beam to produce many diffracted rays (each of them monochromatic) from a crystal of any orientation, without rotating the sample. It was recently adapted to probe the local orientation and deviatoric strain of single grains near the surface of a polycrystalline sample, by using a microfocused white beam ($<1 \times 1\ \mu m^2$, 5–30 keV). 2D maps can then be obtained by translating the sample with respect to the beam.

The methodology was first developed by the group of G.E. Ice at the APS and by the group of N. Tamura at the ALS (Berkeley, CA, USA), and more recently by the group of F. Rieutord on the CEA-CNRS BM32 beamline at ESRF.

Variations of the technique offer additional information. A 3D version adds spatial resolution along the beam by scanning a knife-edge between the sample and the detector. A "full strain tensor" version adds lattice expansion by measuring the energy of a Laue peak, on a grain's volume element for which the white beam Laue pattern was already measured and analyzed for orientation and deviatoric strain. Advanced analysis of spot shapes (and not only spot average positions) adds information about local orientation/strain distribution functions and about dislocation orientation and densities [30] from a fit with a model of defect arrangement.

A typical diffraction geometry is shown in Figure 11.7a, with the distance/angles taken from the BM32 setup [31]. The white beam (divergence 0.5 mrad V $\times$ 1 mrad H) arrives on the sample with an angle around 40°, and the diffracted beams are collected over a solid angle of about 100°, by a 2D detector centered on $2\theta = 90°$ (pixel size 80 μm). Figure 11.7b shows a "single grain" Laue pattern with many spots.

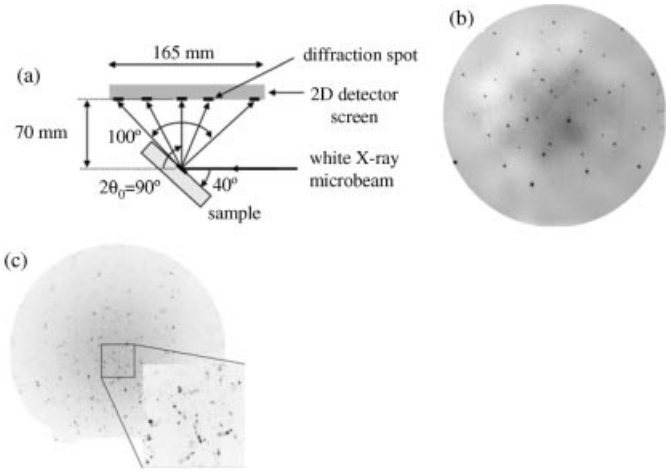

Figure 11.7 (a) Laue microdiffraction geometry (b + c) Laue patterns: "single grain" Cu (b) and "multigrains" W (c).

For accurate strain analysis, the experimental geometry (direction of incident beam and 3D position of the point of impact on the sample, in the detector coordinate system) is first calibrated using the Laue pattern of a Ge strain-free single crystal. After prealigning the sample with a microscope to put the same position of the point of impact along the beam as on the Ge calibration crystal, Laue patterns from the sample are collected. Sample preparation usually involves mechanical polishing, as low surface roughness (<few micrometers) is needed to maintain a constant calibration when translating the sample parallel to its surface for 2D mapping, followed by chemical etching to remove the surface crystal damage induced by polishing.

For the analysis of the sample's Laue pattern, the spot positions, the calibration, and the (known) undeformed unit cell parameters and crystal structure are used, first to index the spots of each grain and second to refine eight of the nine coordinates of the (**a**, **b**, **c**) lattice vectors expressed in the detector axes. These eight parameters are then split into orientation (three Euler angles) and deviatoric strain (b/a, c/a, α, β, γ).

Spot indexation may be involved, as all the illuminated grains inside the beam path may diffract, producing "multigrain" patterns (Figure 11.7c). These can be indexed up to ≈20 grains per pattern. Sensitivity to small grains increases with crystalline perfection and atomic number. The probed depth is spot-dependent: each spot has its own incident beam energy(ies) and penetration depth(s) that can vary from a few micrometers to a few millimeters [32]. This variation in calibration between spots is usually neglected in the analysis or solved by excluding the high-energy spots.

The accuracy of deviatoric strain relies on statistics over several independent determinations: the positions of 4 well-chosen spots (with 3×3 linearly independent **q**-vectors) are necessary and sufficient to derive the 8 parameters, but at least 10–12

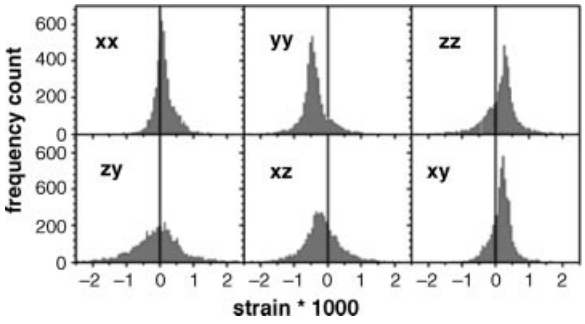

Figure 11.8 Histograms of 4-spot results for deviatoric strain components, from the 32-spot Laue pattern of a micrometer-sized W grain. *x*, *y* are parallel and *z* is perpendicular to the sample surface. Of the three *xx*, *yy*, and *zz* components, only two are independent, the sum being fixed at zero.

peaks (giving more than 50 "good" spot quadruplets) are needed to reach the desired accuracy, between ± 1 and $\pm 2.10^{-4}$ (depending on strain components). Several measures of the data set quality can be built. The simplest is the difference, averaged over the N peaks of a grain, between experimental and theoretical spot positions on the detector, which should be 0.2–0.25 pixels (i.e., 0.2–0.3 mrad in 2θ) for reliable strain determination. Another is the width of the histograms (Figure 11.8) describing the strain results for all the four-spot determinations.

Special caution is needed for multigrain patterns involving grains linked by twinning relations. Spots common to several twins ("multitwin" spots) may be inconsistent in position with the monotwin spots of the crystal under analysis. Indeed, perfectly superimposed spots at zero strain may split when strain alters the orientation relation between the twins.

The Laue patterns provide only five of the six components of the strain tensor, with the lattice expansion missing. This is readily explained (Figure 11.9): the white beam arriving under an angle θ on a given (HKL) plane with interreticular distance d_{HKL} will produce a diffracted beam if the incident spectrum contains a wavelength λ that

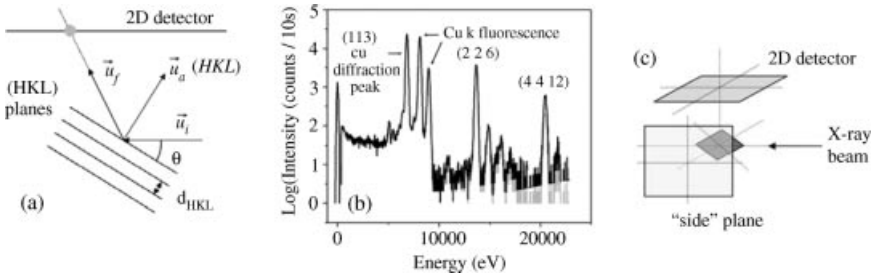

Figure 11.9 (a) Construction of diffracted beams, (b) experimental energy spectrum of a "side" peak (gray: raw data; black: corrected for detector efficiency), and (c) the 2D detector is in the "top" position above the sample, the energy-resolved point detector travels in the "side" plane.

verifies 2 $d_{HKL} \sin\theta = \lambda$. The diffracted beam direction is given by its unit vector $\mathbf{uf} = \mathbf{ui} + 2 \cdot \sin\theta \cdot \mathbf{uq}$, **ui** and **uq** being unit vectors along the incident beam and the diffraction vector $\mathbf{q} = H \cdot \mathbf{a}^* + K \cdot \mathbf{b}^* + L \cdot \mathbf{c}^*$, respectively. If the lattice expands changing only the length of **q** but not the direction of **uq**, θ and **uf** will remain constant, and the spot will stay at the same place on the detector, with only a change in the diffracted wavelength, to match the change in d_{HKL}. The spot positions in the Laue pattern are therefore insensitive to small changes in lattice expansion: they are sensitive only to changes in lattice rotation and deviatoric strain, which change the direction of **uq**. Note that the same spot may contain several harmonics, (*HKL*) at E_0, (2H 2K 2L) at $2E_0$, and so on, and therefore mix several probing depths.

The lattice expansion is given by the difference between the experimental spot energy Eexp_{HKL} and the theoretical spot energy at zero lattice expansion Etheor_{HKL}. Etheor_{HKL} is calculated from the grain's orientation and deviatoric strain experimentally found using the Laue pattern. Illuminating exactly the same volume inside the grain for the two measurements (of the Laue pattern – giving Etheor – and of Eexp) is therefore mandatory, especially as Etheor varies very quickly with lattice rotation.

The first technique to measure lattice expansion is to monochromatize the incident beam and scan its energy around Etheor_{HKL}, while recording the *HKL* spot on the 2D detector, to find the energy giving the maximum intensity [23]. Ideally, the experimental energies of several spots per volume element inside a grain should be measured. This implies several realignments of the beamline optics and checks of the beam size and position with respect to the sample, except if spots with similar energies (within 1 keV) can be used.

The second technique is to collect "side" Laue peaks in the white beam mode, using an energy-resolved point detector mounted on two translation stages [33]. This allows to simultaneously measure the "top" Laue pattern with the 2D detector and the energy spectrum of a "side" Laue peak (Figure 11.9b and c), ensuring that Etheor and Eexp are measured under the same illumination conditions. To reach the desired accuracy on peak energy, the detector's energy channel relation is recalibrated at each spectrum using the sample's main fluorescence line. Measured energies are also corrected for the variations of E(ch) with the detector's total intensity. The resolution-limited ≈200 eV-wide peaks are measured with ≈20 eV channels, and peak fitting achieves a resolution of ≈0.1 eV channel on peak position for peaks with a symmetric shape.

To add spatial resolution along the beam, one uses a triangulation/ray-tracing method called "differential aperture X-ray microscopy" described in Figure 11.10. A thin absorbing wire is translated with submicron accuracy parallel and close to the sample surface, and successively masks the various diffracted beams. In materials with small grains, this allows to sort simultaneously illuminated grains according to their depth below the surface. The center of mass of a grain's illuminated volume is located by ray tracing of the diffracted beams. The ray is traced using the average position of the spot on the detector and the y-position of the wire to cut half the spot intensity. This ray tracing is precise close to the sample, thanks to the large ratio between the sample detector and sample wire distances.

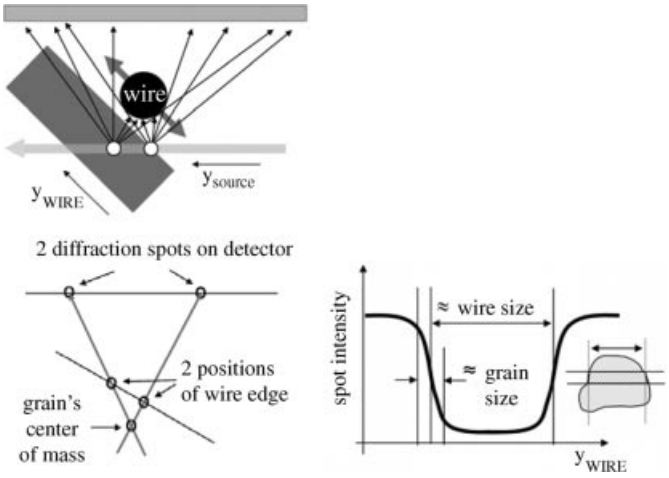

Figure 11.10 Geometry of the wire-scanning technique. The proportions are not respected: the real sample–detector distance is typically 200 times bigger than the wire–sample distance (few 100 μm). The wire (diameter 50 μm) acts as a knife edge that masks the diffracted beams.

In materials with bigger grains showing intragrain strain or orientation distribution (and therefore elongated spots), the technique allows to measure the gradient along the beam of the strain/orientation matrix. Here the analysis is more involved: the problem is to reconstruct a list of spot positions specific to a given crystal slice located at a distance y_{source} below the surface. This is achieved by analyzing spot positions in the difference images, each obtained by subtracting the image at y_{wire} from the image at $y_{wire} + dy$. From a difference image in which a portion of spot N is visible (i.e., corresponding to a y_{wire} for which the wire partially masks this spot), the source of the partial spot is located by tracing the fan from the partial spot position to the wire edge position, and crossing with the (known) incident beam. This allows to classify partial spots from all different images according to their source position, and to reconstruct the slice-specific spot lists. This method requires high stability of beam intensity and position during the scan.

Rough arguments for choosing which technique is best adapted to a given sample are given below. 3DXRD is faster for getting a grain-center-of-mass 3D structure, but needs bigger grains (>5 μm). Grain boundary mapping with 3DXRD works best for well-crystallized materials. Laue microdiffraction is able to handle smaller grains (down to 0.1 μm if well crystallized) and larger degree of intragrain plastic strain (but not the two at the same time). Elastic strain measurements are comparatively more straightforward for Laue microdiffraction but the lattice expansion is rarely measured, in contrast with 3DXRD that maps the full tensor. The two techniques require well-crystallized grains for elastic strain measurements. Full 3D Laue microdiffraction is slow.

Developments point toward faster detectors with smaller pixels and smaller beams, as well as handling the analysis for sample with larger intragrain plastic strain.

11.5
Local Strains Derived from the Intensity Distribution in Reciprocal Space

11.5.1
Periodic Assemblies of Identical Objects with Coherence Length > Few Periods

11.5.1.1 Introduction

Since the lateral dimension of electron devices is continuously decreasing, stress engineering is becoming of rising interest to enhance microelectronic device performance in particular by improving electron or hole mobility in strained silicon channel [34, 35]. As a consequence, mapping the strain induced in silicon single crystal at the nanometer scale is an important requirement but remains a real challenge.

In the particular case of single crystals, one way to achieve the nanometer resolution is to use X-Ray diffraction with a wide beam (hence with a size larger than the coherence length) and quasiparallel beam, which requires working under high-resolution conditions [36–38]. The resolution in the object space is reached through the study of reciprocal space maps (RSMs) of the intensity in the Fourier space. These maps are very sensitive to local strains ($<10^{-4}$) [39–41].

Periodic structures are often encountered in real semiconductor devices, whether they are prepared by lithography or by self-organization. They can also be made on purpose, in order to get more scattered amplitude. X-Ray measurements are thus performed on periodic assemblies of identical objects. The periodicity induces a Fourier pattern where the intensity of each Fourier component is related to the amplitude scattered by a single cell. In practice, the periodic strain field induced in single-crystal silicon yields satellites in reciprocal space around Si Bragg peaks. The intensities of these satellites represent a fingerprint of the strain field in the silicon substrate.

For example, an array of trenches etched in silicon and filled with silicon oxide gives rise to satellites in the reciprocal space around the Si(404) Bragg peak [40] (see Figure 11.13a), their intensity being directly linked not only to the geometrical shape of the Si lines between the trenches but also to the local strain field induced in Si by the filling material. The satellites spacing is inversely proportional to the period (Figure 11.13c).

It is, however, not possible to invert directly the diffracted intensity to deduce the strain field because the phase information is lost by measuring the square modulus of the amplitude (under some particular conditions, the phase may be numerically retrieved as explained in Section 11.6). As a consequence, the displacement field is first simulated and used for calculations of the diffracted intensity maps in reciprocal space. The displacement field can be either calculated by solving an analytical mechanical model [42] or extracted from a finite element (FE) modeling [43]. The comparison between the experimental and the calculated reciprocal space maps, tuning the mechanical loading of the materials, allows for the validation of the induced strain field in the silicon [43, 44].

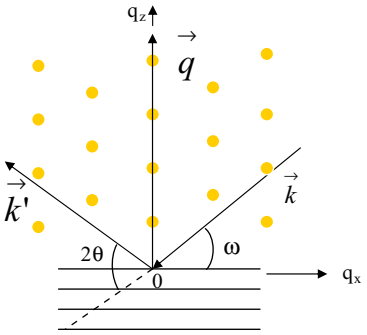

Figure 11.11 Reciprocal space of a (001) cubic crystal with [100] orientation. The vector $\vec{k}_i$ is the incident wave vector and $\vec{k}_f$ is the scattered one.

11.5.1.2 Reciprocal Space Mapping

The reciprocal space is the Fourier representation of the crystal, each family of crystalline planes being represented by a node called Bragg peak (Figure 11.11). The scattering vector q is perpendicular to the crystal planes under Bragg conditions. The axis called *qx*, *qy*, and *qz* correspond to the components of the scattering vector as defined in Eq. (11.2). For an *HKL* reflection, they write

$$q_x = q_y = \frac{4\pi}{\lambda}\sin\theta\sin(\theta-\omega) \quad \text{and} \quad q_z = \frac{4\pi}{\lambda}\sin\theta\cos(\theta-\omega) \tag{11.13}$$

where the angles θ and ω correspond, respectively, to the diffracted and to the incident angles with respect to the crystal plane (Figure 11.11).

In practice, the measurements are performed by scanning a small area around the unstrained silicon substrate Bragg peak, for a chosen *HKL* reflection. The key factor in such a measurement is the resolution within the reciprocal space. The use of an analyzer (three-reflection Si or Ge monocrystals) between the sample and the detector allows for decreasing the acceptance angle. The detector is usually one dimensional.

Two series of scans have to be defined in order to reconstruct the reciprocal space map.

Depending on the software, one can either monitor the *qx*- and *qz*-values for mapping directly the reciprocal space or monitor the motor 2θ and ω angular values and then calculate the *qx*- and *qz*-values to plot the map. The ω–2θ scan corresponds to a variation in the exit angle being twice the incident angle ω value. The ω scans (called "rocking curve") are perpendicular to the ω–2θ ones in the reciprocal space. Typically, for an angular step equal to 0.003°, the corresponding step in reciprocal space is $0.004\,\text{nm}^{-1}$ at the wavelength of Cu Kα radiation.

In order to extract normal strains along the three directions, both symmetric and asymmetric Si reciprocal space maps are necessary. In the symmetrical geometry, the scattering vector has only a vertical component q_z because the incident wave vector $\vec{k}_i$ and scattered wave vector $\vec{k}_f$ are symmetric with respect to the *y*-direction. A tensile strain ($\varepsilon_{zz} > 0$) along the vertical direction shifts the scattered intensity to lower q_z

values in reciprocal space, while a compressive strain ($\varepsilon_{zz} < 0$) is associated with higher q_z values. In the asymmetrical geometry, vertical and horizontal components of the scattering vector q_x and q_z yield information about the horizontal strain.

Experimental Setup In a high-resolution setup, a monochromator is necessary to reduce the wavelength spread and get a parallel incident beam, followed by an analyzer to achieve the required angular resolution [45, 46]. A major advantage of this methodology is that the measurements on periodic arrays on silicon can be often performed by using a laboratory instrument.

For example, at IM2NP laboratory in Marseille, a 4-circle goniometer with a sealed Cu X-ray tube and a 3-bounce Ge 220 analyzer is used for high-resolution measurements. Two setups are available for the monochromator. The first one is a 4-bounce Ge(220) symmetrical DuMond-Bartels monochromator used with a point focus, which presents a low divergence in the scattering plane (12 arcsec). With this setup, both monochromator and analyzer streaks are reduced and almost not visible in the reciprocal space maps (Figure 11.13a). This setup is needed for large period arrays (around 1 μm), and because the satellites get closer in the reciprocal space, the highest resolution is necessary [47]. The second setup is a 2-bounce Ge(220) associated with a parabolic variable-step multilayer mirror used in line focus. The intensity is thus increased by a factor of 20 that is absolutely necessary when measuring large maps (structures with submicrometric period) with a good signal/noise ratio [48]. The drawback is an incident beam divergence around three times larger than the previous one and the monochromator streak more visible on the maps [49] (see Figure 11.12). In some cases, a more brilliant source might be necessary and is achieved with synchrotron radiation. For example, the BM32 line at ESRF is equipped with a double-crystal Si(111) monochromator and a triple-bounce Si(111) analyzer may be used [43, 46, 47].

Modeling Let us consider the general case of a line adherent on a silicon substrate. When the displacement field is known at each lattice point, the intensity map can be determined with the kinematical [50] or dynamical theories [51].

The displacement values within the structure are usually determined through finite elements modeling (FEM). In a few simple cases, it can also be calculated using an analytical approach [42, 52–54]. FEM is a numerical method to solve partial differential equations, here the Navier–Lamé equations. It consists in a discretization of the structure by a finite number of elements with a simple geometrical shape, and connected with nodes. The continuous medium is thus converted in discrete areas, with a finite number of unknown quantities that are the displacement values.

In the particular case of periodic arrays, a single cell is simulated with boundary conditions (lateral borders blocked along x-direction, which is perpendicular to the line direction). The periodic structures are considered as infinite along the y-direction. Plane strain (in the x–z-plane) is assumed in silicon (but not in the stressor line), which simplifies the problem to a 2D analysis. Mechanical parameters E, ν, α, and C_{ij} are introduced for the different materials. The initial stress is introduced in the materials through an artificial thermal loading ΔT since

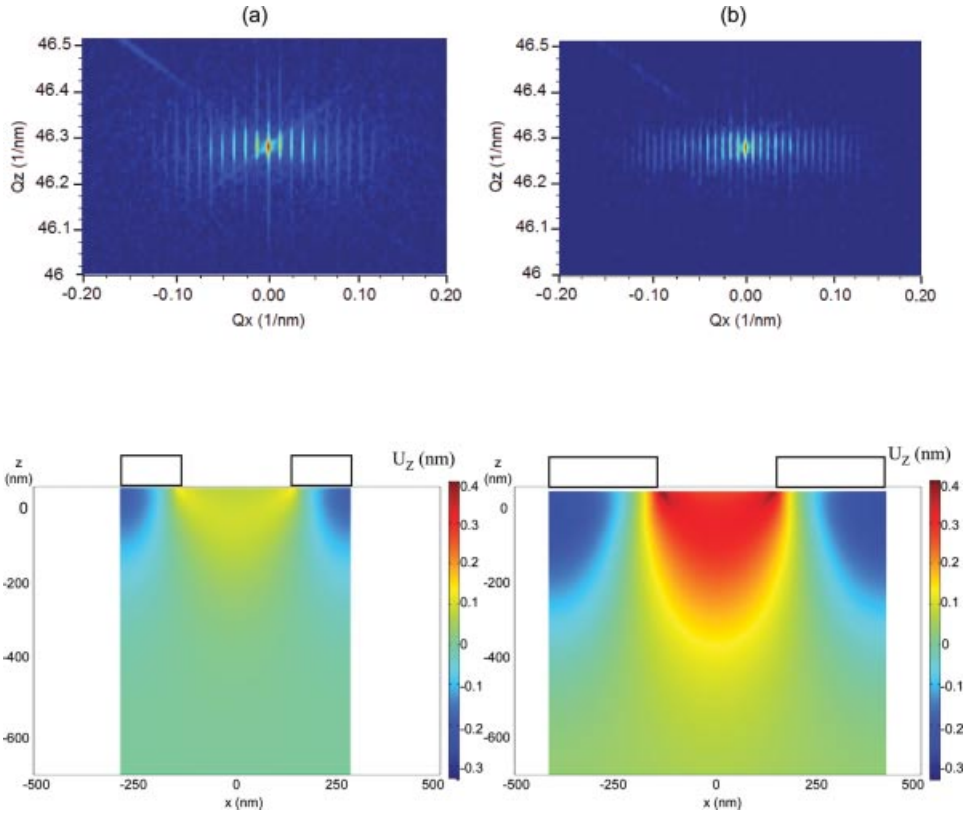

Figure 11.12 Experimental (004) reciprocal space maps for Si capped by an array of nitride lines, with same spacing = 250 nm and (a) width = 250 nm or (b) width = 500 nm. Below are represented the corresponding vertical displacement fields extracted from FEM. Bare Si is at the center, the nitride line is separated into two parts on each side.

$$\sigma_0 = \frac{E}{1-\nu}\Delta\alpha^*\Delta T \tag{11.14}$$

where $\Delta\alpha$ is the thermal expansion coefficient difference between the considered material and the silicon (reference), E and ν are the elastic coefficients (Young's modulus and Poisson ratio) of the line material (considered here isotropic), and σ_0 is the residual stress in the line material (prior to any elastic relaxation).

The displacement field values obtained with FEM at each node j are then used to calculate the expected diffracted intensity: within kinematical approach and Takagi [14] approximation a simple Fourier transform is needed (see Eq. (11.8)).

11.5.1.3 **Applications**

The periodic array can be either deposited on top of the single crystal or directly created within the Si by etching and filling trenches. When the periodic array is

deposited on top of the Si substrate without any etching, the periodicity measured on the reciprocal space is solely caused by the strain field periodicity. For example, silicon nitride lines are periodically deposited single-crystal (001) Si substrates [55]. The effect of the silicon nitride stressor was shown on two sets of the sample. In the case of model bare nitride arrays, the strain field was simulated with the help of FEM. The diffracted intensity was calculated for the symmetrical (004) reflection, and adjusted with the experimental one as shown in Figure 11.12. The best agreement with measurement was found for an initial stress $\sigma_o = 1.5$ GPa in the nitride lines, giving a maximum vertical strain value $\varepsilon_{zz} = -1\ 10^{-3}$ in the silicon below the lines. This maximum value extends two times deeper into the silicon for a line two times larger (see Figure 11.12).

This method has also been applied for measuring the strain in silicon lines, induced by a periodic array of filled trenches. In the submicrometric shallow trench isolation (STI) process, the silicon substrate is etched in pyramidal lines, with the trenches in-between the lines filled with silicon oxide SiO_2. On the asymmetric RSMs, the satellite envelope is clearly not centered on the substrate peak. A secondary maximum is evidenced in addition to the intense diffraction peak attributed to the unstrained Si [40], which suggests there is a large enough amount of silicon with almost constant strain to produce a well-separated diffraction peak in the array satellite envelope. On asymmetric RSMs (Figure 11.13), the diffracted signal is clearly shifted to lower value of L and to higher value of H that corresponds to compressive strain across Si lines and tensile strain vertically [47]. The secondary peak was interpreted, with the help of FEM calculations, as arising from a homogeneously strained area in the Si lines where ε_{xx} and ε_{zz} values remain stable vertically on half the depth and laterally on half the width of the lines [49]. In the particular case of a homogeneously strained area, the strain value can be directly extracted from the secondary peak position in the experimental map. In practice, the normal strains ε^0_{xx} and ε^0_{zz} are related to the relative position of that peak ΔH and ΔL as compared to the Si substrate Bragg peak (H_0, L_0) along H and L, as follows:

$$\varepsilon^0_{xx} = \frac{\Delta H}{H_0} \quad \text{and} \quad \varepsilon^0_{zz} = \frac{\Delta L}{L_0} \tag{11.17}$$

Stress values are then deduced from the strains via Hooke's law $\sigma_i = C_{ij}\varepsilon_j$.

11.5.2
Single-Object Coherent Diffraction

A small crystal illuminated by a fully coherent beam (i.e., whose longitudinal and transverse coherence lengths are larger than the diffracting crystal) yields a coherent diffraction pattern whose intensity is the square modulus of the amplitude as given in (11.1) or (11.8). Streaks perpendicular to the crystal facets and thickness fringes are typical of coherent diffraction patterns related to the shape function of the crystal. As shown in (11.8) strains may have a large influence on the diffraction pattern; see also Figure 11.1). Figure 11.14 shows the coherent diffraction pattern from a single

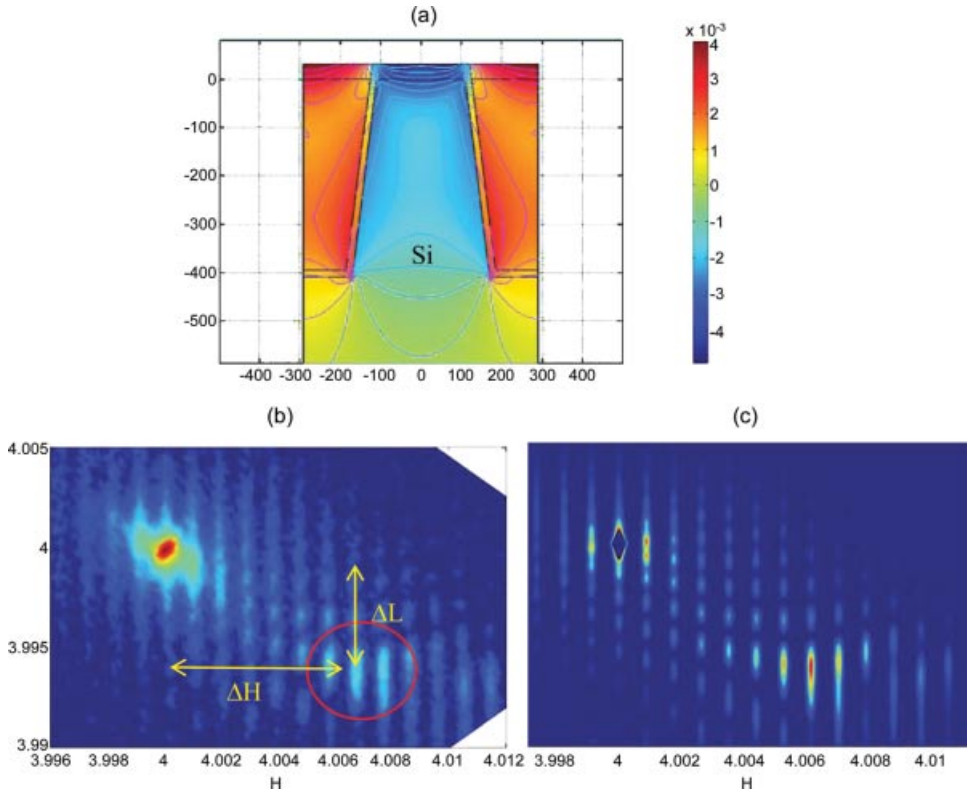

Figure 11.13 (a) Strain field ε_{zz} calculated by FEM. The iso-strain lines are separated by $\pm 0.45^{*}10^{-3}$. The *x*- and *z*-axes are in nanometer. Si line is located between the two half trenches. (404) silicon reciprocal space maps: (b) on the left laboratory measurement, (c) on the right FEM simulation. The secondary peak is red rounded on measurement.

Au grain ($375 \times 200\,\mathrm{nm}^2$) within a polycrystalline thin film [56]. The 111 reflection shown here corresponds to lattice planes parallel to the film surface. Fringes along the 2θ direction are clearly visible. Moreover, the diffraction pattern shows a clear asymmetry, which is a fingerprint for the presence of strain. The 004 diffraction pattern from Si lines [43] shown in Figure 11.15 is even more striking. Along the *qz*-direction perpendicular to the surface, finite size fringes are inversely related to the Si thickness. Along the transverse direction, a large broadening is observed together with aperiodic fringes. This is completely dominated by the strain gradient present in the line. Finite element modeling of the displacement field in the line yields a diffracted intensity, which is in very good agreement with the measured one [43]. Since the phase of the scattered amplitude is actually not recorded, the determination of the strain in the crystal directly from the measured diffraction pattern remains ambiguous. The phase problem may, however, be circumvented using phase retrieval algorithms as will be discussed in the next section. A good

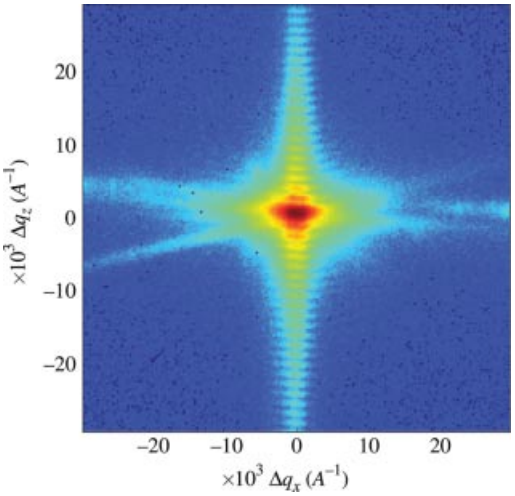

Figure 11.14 111 coherent diffraction pattern from an Au crystal (375 nm × 200 nm) within a polycrystalline film. Adapted from Ref. [56].

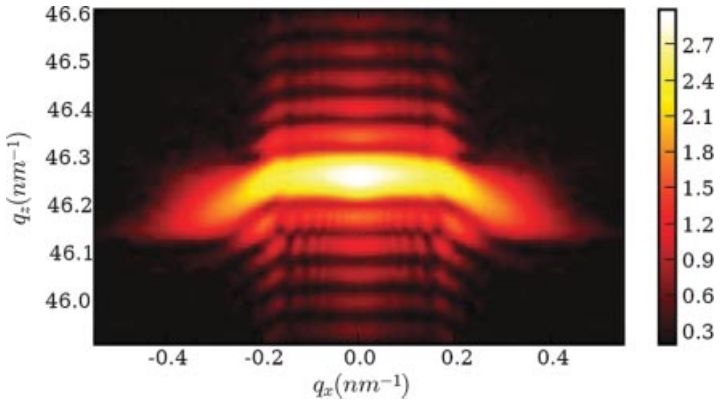

Figure 11.15 004 reciprocal space map from an array of 100 nm × 1 μm Si lines as recorded at ESRF BM32 beam line. Adapted from Ref. [43].

review on the capabilities of coherent diffraction imaging at the nanoscale has been recently published [57].

11.6
Phase Retrieval from Strained Crystals

Since the phase of the scattered amplitude (8) is not measured, one uses generally model-dependent approaches. The square modulus of the Fourier transform from

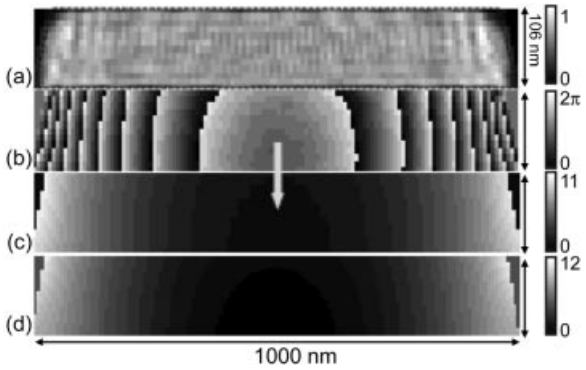

Figure 11.16 Direct inversion via phase retrieval from the diffraction pattern in Figure 11.13: (a) amplitudes (in arbitrary units), which are related to the shape and the density of the Si line; (b) phases (in radians); (c) retrieved displacement field u_z (in Å), (*d*) displacement u_z (in Å) calculated by finite element modeling. Adapted from Ref. [64].

a model structure is compared with the experimental intensity. Direct inversion, based on phase retrieval algorithms, is on the other hand a very promising technique. It is based on the oversampling conception [58], which states that the diffracted intensity pattern should be sampled at a frequency at least twice the highest spatial frequency in the object. The principle of direct inversion algorithms [59, 60] relies on phase retrieval starting from a set of random phases, which are constrained (i) in real space by adding additional information such as finite support for the object and (ii) in reciprocal space by pushing the calculated amplitudes to the measured ones. This approach has been highly successful in retrieving the shape of objects, whether noncrystalline [61] or crystalline [62] from their diffraction pattern. The case of inhomogeneously strained crystals is more challenging. The strain field in a micrometer-sized Pb crystal has been recently [63] retrieved from its diffraction pattern. In this particular case, the maximum phase difference was less than 2π, which implies very small strains, in the 10^{-4} range. Larger strains hinder the convergence of standard algorithms [59, 60]. Recently, a modified algorithm [64, 65] with additional constraints on the derivatives of the displacement field has been successfully implemented. The displacement field in silicon lines is retrieved with a spatial resolution of 8 nm (Figure 11.16) and is in very good agreement with the one deduced from FEM. This result is very promising for the general issue of model-independent determination of strains in nanocrystals.

11.7 Conclusions and Perspectives

This article is a tentative review of recent advances in strain measurements using X-ray diffraction. Thanks to third-generation synchrotrons and continuous progress

being made in the capabilities of X-ray optics, the past 10 years have witnessed important developments in the field of local strain mapping. The availability of small beams is one of the key factors that have allowed for local strain measurements whether through monochromatic or Laue diffraction. These approaches are starting to diffuse within the community of physicists, metallurgists, and mechanical engineers and will soon become almost routine tools for evaluating strains down to submicrometer scales. It is interesting to notice that a 1 μm length of dislocation in $1\,\mu m^3$ translates in a dislocation density of $10^{12}\,m^{-2}$. Hence, these local strain measurement techniques are also drastically changing the way we think about how diffraction averages over strain gradients and defects. Coherent X-ray diffraction, which can map strains in small crystals with a spatial resolution as small as 8 nm, is also extremely promising for looking at mechanical properties of small crystals. Its development is strongly linked with the availability of robust phase retrieval algorithms.

What lies ahead? First of all smaller beams, 50 nm beams have been demonstrated [66–70] and most synchrotron sources in the world are putting a lot of effort to develop nanobeam stations (see, for example, the ESRF upgrade program [71]). One should also follow with attention the possibilities that offer a drastically new kind of X-ray source that is the X-ray free electron laser (XFEL). The first one in the world has recently delivered its first beam at Stanford [72]. In Europe, XFEL is expected to deliver its first beam in Hamburg by 2014 [73]. These new X-ray sources will offer a tremendous gain in photon flux (there are actually concerns about beam damage) together with very high transverse coherence.

References

1 Noyan, I. and Cohen, J. (1987) *Residual Stress: Measurement by Diffraction and Interpretation*, Springer, New York.

2 Bergemann, C., Keymeulen, H., and van der Veen, J. (2003) *Phys. Rev. Lett.*, **91**, 204801.

3 Tamura, N., Celestre, R., MacDowell, A., Padmore, H., Spolenak, R., Valek, B., Meier Chang, N., Manceau, A., and Patel, J. (2002) *Rev. Sci. Instrum.*, **73**, 1369.

4 Fewster, P.F. (2003) *X-Ray Scattering from Semiconductors*, Imperial College Press.

5 Freund, L. and Suresh, S. (2004) *Thin Film Materials: Stress, Defect Formation and Surface Evolution*, Cambridge University Press.

6 Thomas, O., Shen, Q., Schieffer, P., Tournerie, N., and Lepine, B. (2003) *Phys. Rev. Lett.*, **90**, 017205.

7 Ogawa, E.T., McPherson, J.W., Rosal, J.A., Dickerson, K.J., Chiu, T.-C., Tsung, L.Y., Jain, M.K., Bonifield, T.D., Ondrusek, J.C., and McKee, W.R. (2002) *Stress induced voiding under vias connected to wide Cu metal leads*, 40th Annual Proceedings: International Reliability Physics Symposium, p. 312.

8 Thompson, S.E., Armstrong, M., Auth, C., Cea, S., Chau, R., Glass, G., Hoffman, T., Klaus, J., Ma, Z., Mcintyre, B. *et al.* (2004.) *IEEE Trans. Electron. Devices Lett.*, **25**, 191.

9 Warren, B. (1991) *X-Ray Diffraction*, Dover.

10 Authier, A. (2001) *Dynamical Theory of X-Ray Diffraction*, Oxford University Press.

11 Thomas, O. (2007) *Z. Kristallogr.*, **223**, 569.

12 Giacovazzo, A. (2002) *Fundamentals of Crystallography*, Oxford University Press.

13 Landau, L. and Lifshitz, E. (1967) *Theory of Elasticity*, Mir.
14 Takagi, S. (1969) *J. Phys. Soc. Japan*, **26**, 1239.
15 Putero, M. (1996) PhD thesis, Univ. Aix-Marseille III.
16 Labat, S., Gergaud, P., Thomas, O., Gilles, B., and Marty, A. (2000) *J. Appl. Phys.*, **87**, 1172.
17 Gergaud, P., Baldacci, A., Rivero, C., Sicardy, O., Boivin, P., Micha, J.-S., and Thomas, O. (2006) *Stresses in copper damascene lines : In situ measurements and finite element analysis.*, Stress-Induced Phenomena in Metallization: Eighth International Workshop on Stress-Induced Phenomena in Metallization AIP Conference Proceedings, **817**, p. 205.
18 Welzel, U. and Mittemeijer, E. (2007) *Z. Kristallogr.*, **222**, 160.
19 Mittemeijer, E.J. and Scardi, P. (2004) *Diffraction Analysis of the Microstructure of Materials*, Springer, Berlin.
20 Lauridsen, E.M., Schmidt, S., Sutter, R.M., and Poulsen, H.F. (2001) *J. Appl. Crystallogra.*, **34**, 744.
21 Poulsen, H.F. (2008) *Three-Dimensional X-Ray Diffraction Microscopy, Tracts in Modern Physics*, Springer p. 205.
22 Chung, J.-S. and Ice, G.E. (1999) *J. Appl. Phys.*, **86**, 5249.
23 Ice, G.E., Chung, J.-S., Lowe, W., Williams, E., and Edelman, J. (2000) *Rev. Sci. Instr.*, **71**, 2001.
24 http://sourceforge.net/apps/trac/fable/wiki.
25 Poulsen, H.F., Nielsen, S.F., Lauridsen, E.M., Schmidt, S., Suter, R.M., Lienert, U., Margulies, L., Lorentzen, T., and Juul Jensen, D. (2001) *J. Appl. Crystallogra.*, **34**, 751.
26 http://www.im2np.fr/GDR-Mecano/grenoble2009/Wright.pdf.
27 Markussen, T., Fu, X., Margulies, L., Lauridsen, E.M., Nielsen, S.F., Schmidt, S., and Poulsen, H.F. (2004) *J. Appl. Crystallogra.*, **37**, 96.
28 Poulsen, H.F. and Schmidt, S. (2003) *J. Appl. Crystallogra.*, **36**, 319.
29 Poulsen, H.F. (2003) *Phil. Mag.*, **83**, 2761.
30 Ice, G.E. and Barabash, R.I. (2007) *Dislocations in Solids* (eds F.R.N. Nabarro and J.P. Hirth), Elsevier, pp. 499–601.
31 Ulrich, O., Biquard, X., Bleuet, P., _Geaymond, O., Gergaud, P., Micha. J.S., and Robach, O. (2011) *Rev. Sci. Instrum.*, **82**, 033908.
32 http://henke.lbl.gov/optical_constants/atten2.html.
33 Robach, O., Micha, J.-S., Ulrich, O., and Gergaud, P., *J. Appl. Crystallogra.*, in press.
34 Arghavani, R., Yuan, Z., Ingle, N., Jung, K.-B., Seamons, M., Venkataraman, S., Banthia, V., Lilja, K., Leon, P., Karunasiri, G., Yoon, S., and Mascarenhas, A. (2004.) *IEEE Trans. Electron. Devices*, **51**, 1740.
35 Sun, Y., Sun, G., Parthasarathy, S., and Thompson, S.E. (2006) *Mater. Sci. Eng. B*, **135**, 179.
36 Caro, L.D. and Tapfer, L. (1994) *Phys. Rev. B*, **49**, 11127.
37 Shen, Q., Kycia, S.W., Tentarelli, E.S., Schaff, W.J., and Eastman, L.F. (1996) *Phys. Rev. B*, **54**, 16381.
38 Tolan, M., Press, W., Brinkop, F., and Kotthaus, J.P. (1994) *J. Appl. Phys.*, **75**, 7761.
39 Baumbach, T., Lübbert, D., and Gailhanou, M. (2000) *Mater. Sci. Eng. B*, **69–70**, 392.
40 Eberlein, M., Escoubas, S., Gailhanou, M., Thomas, O., Rohr, P., and Coppard, R. (2006) *Mater. Res. Soc. Symp. Proc.*, **913**, D05-02.
41 Shen, Q. and Kycia, S. (1997) *Phys. Rev. B*, **55**, 15791.
42 Kaganer, V.M., Jenichen, B., Paris, G., Ploog, K., Konovalov, O., Mikulik, P., and Arai, S. (2002) *Phys. Rev. B*, **66**, 035310.
43 Gailhanou, M., Loubens, A., Micha, J.-S., Charlet, B., Minkevich, A.A., Fortunier, R., and Thomas, O. (2007) *Appl. Phys. Lett.*, **90**, 111914.
44 Eberlein, M., Escoubas, S., Gailhanou, M., Thomas, O., Rohr P., and Coppard, R. (2008) T*hin Solid Films*, **516**, 8042–8048.
45 Holy, V., Pietsch, U., and Baumbach, T. (1999) *High Resolution X-Ray Scattering from Thin Films and Multilayers*, vol. 149, Springer Tracts in Modern Physics, Springer.
46 http://xfel.desy.de/.
47 Eberlein, M., Escoubas, S., Gailhanou, M., Thomas, O., Micha, J.-S., Rohr, P., and

Coppard, R. (2007) *Phys. Stat. Sol. (a)*, **204** (8), 2542.
48 Escoubas, S., Brillet, H., Mesarotti, T., Raymond, G., Thomas, O., and Morin, P. (2008) *Mater. Sci. Eng. B*, **154–155**, 129.
49 Escoubas, S., Eberlein, M., Rohr, P., and Thomas, O. (2009) *Mater. Sci. Semicond. Process.*, **12** (1–2), 64.
50 Azaroff, L.V., Kaplow, R., Kato, N., Weiss, R.J., Wilson, A.J.C., and Young, R.A. (1974) *X-Ray Diffraction*, McGraw-Hill, New York.
51 Stepanov, S.A., Pietsch, U., and Baumbach, G.T. (1995) *J. Phys. B. Cond. Matter*, **96**, 341.
52 Hu, S.M. (1978) *Appl. Phys. Lett.*, **32**, 5.
53 Hu, S.M. (1978) *J. Appl. Phys.*, **50**, 7.
54 Hu, S.M. (1991) *J. Appl. Phys.*, **70**, R53.
55 Escoubas, S., Gaudeau, G., Ezzaidi, Y., Thomas, O., and Morin, P. (2011) *J. Nanosci. Nanotechnol.*, **11**, in press.
56 Vaxelaire, N., Proudhon, H., Labat, S., Kirchlechner, C., Keckes, J., Jacques, V., Ravy, S., Forest, S., and Thomas, O. (2010) *New J. Phy.*, **12**, 035018.
57 Robinson, I. and Harder, R. (2009) *Nat. Mater.*, **8**, 291.
58 Sayre, D. (1952) *Acta Cryst.*, **5**, 843.
59 Fienup, J. (1982) *Appl. Opt.*, **21**, 2758.
60 Gerchberg, R. and Saxton, W. (1972) *Optik*, **35**, 237.
61 Miao, J., Charalambous, P., Kirz, J., and Sayre, D. (1999) *Nature*, **400**, 342.
62 Robinson, I., Vartanyants, I., Williams, G., Pfeifer, M., and Pitney, M. (2001) *Phys. Rev. Lett.*, **87**, 195505.
63 Pfeifer, M., Williams, G., Vartanyants, I., Harder, R., and Robinson, I. (2006) *Nature*, **442**, 63.
64 Minkevich, A., Gailhanou, M., Micha, J.-S., Charlet, B., Chamard, V., and Thomas, O. (2007) *Phys. Rev. B*, **76**, 104106.
65 Minkevich, A., Baumbach, T., Gailhanou, M., and Thomas, O. (2008) *Phys. Rev. B*, **78**, 174110.
66 Chao, W., Hartenaeck, B., Liddle, J., Anderson, E., and Attwood, D. (2005) *Nature*, **435**, 1210.
67 Hignette, O., Cloetens, P., Rostaing, G., Bernard, P., and Morawe, C. (2005) *Rev. Sci. Instrum.*, **76**, 063709.
68 Pfeiffer, F., David, C., Burghammer, M., Riekel, C., and Salditt, T. (2002) *Science*, **297**, 230.
69 Schroer, C. and Lengeler, B. (2005) *Phys. Rev. Lett.*, **94**, 054802.
70 Schroer, C., Kurapova, O., Patommel, J., Boye, P., Feldkamp, J., Lengeler, B., Burghammer, M., Rieckel, C., Vincze, L., van der Hart, A., and Küchler, M. (2005) *Appl. Phys. Lett.*, **87**, 124103.
71 http://www.esrf.eu/AboutUs/Upgrade.
72 https://slacportal.slac.stanford.edu/sites/lcls_public.
73 Schroer, C., Boye, P., Feldkamp, J., Patommel, J., Schropp, A., Schwab, A., Stephan, S., Burghammer, M., Schöder, S., and Riekel, C. (2008) *Phys. Rev. Lett.*, **101**, 090801.